Nanoscale Advances

ROYAL SOCIETY OF CHEMISTRY

PAPER

View Article Online
View Journal | View Issue

Cite this: *Nanoscale Adv.*, 2026, **8**, 1762

Plant-extract-mediated synthesis of copper oxide nanoparticles for sustainable lead detoxification: experimental evaluation and docking studies

Nabila Shehata,[a] Simranjeet Singh,†[b] Radhika Varshney,[b] Pavithra N,[b] Daljeet Singh Dhanjal[b] and Praveen C. Ramamurthy *[b]

Increasing levels of water pollution involving heavy metals have demanded the exploration and development of efficient, sustainable approaches for the decontamination of these pollutants. In this study, copper oxide nanoparticles (CuO NPs) were synthesized using *Haldina cordifolia* for the removal of a persistent heavy metal from water. Advanced characterization analyses confirm both their successful synthesis and their distinctive adsorption characteristics toward Pb(II) from water. The highest-ranked docked conformation attained in molecular docking simulations showed a binding energy of −0.36 kcal mol^{-1}. The negative binding energy attained indicates a favourable affinity of the CuO NPs towards $Pb(NO_3)_2$. The maximum adsorption capacity of Pb(II) onto CuO NPs is 1032.57 mg g^{-1} under the optimum conditions (pH 6, dose 50 g L^{-1}, and contact time 2 h). The adsorption mechanism is driven by both chemical (complexation, precipitation, and ion exchange) and physical electrostatic attractions. The kinetic study reveals that five kinetic models, namely, pseudo-first-order, pseudo-second-order, mixed first- and second-order, Avrami, and intraparticle diffusion, can describe the adsorption of Pb(II) onto CuO NPs, depending on the initial Pb(II) concentration. Adsorption isotherm modelling shows that among the eleven models studied, Freundlich isotherm best describes the adsorption system, with strong agreement between experimental and calculated data. Future research can thus focus on enhancing the synthesis process while examining the selectivity and reusability of CuO NPs for decontaminating the diverse metals present in intricate wastewater systems.

Received 4th November 2025
Accepted 25th January 2026

DOI: 10.1039/d5na01027f

rsc.li/nanoscale-advances

1 Introduction

Freshwater scarcity remains a pressing global concern that has significant consequences for the well-being of humans and societal development. According to the 2023 UNESCO assessment, around 2 billion individuals, approximately 26% of the global population, lack access to a reliable supply of potable water.[1] The UNESCO report further highlights that around 2–3 billion individuals worldwide are currently experiencing water scarcity. This issue of water scarcity is anticipated to worsen in the forthcoming decades.[2] Moreover, recent forecasts indicate that approximately half of the world's population is likely on the verge of experiencing risks and threats associated with water scarcity.[3] Amid the persistent freshwater scarcity, heavy metal contamination has emerged as a significant environmental issue.[4] These toxic elements increasingly enter aquatic ecosystems through effluents derived from different industrial processes, mining activities, and insufficient wastewater treatment, which result in their accumulation in soils and surface waters.[5] Elevated concentrations of heavy metals in aquatic systems pose severe risks to both human populations and ecological integrity, especially when levels exceed the permissible environmental thresholds. These contaminants persist in the environment after they are released because of their non-biodegradable nature and the limited removal efficiency of conventional wastewater treatment systems.[6] Chronic exposure to these heavy metals is linked to bioaccumulation and biomagnification within food chains, leading to toxicological effects in humans and wildlife. The World Health Organization has categorized heavy metal contamination as one of the important environmental health concerns owing to its contribution to chronic diseases and its potential to jeopardize global public health systems. Additionally, the absorption of heavy metals by plants interferes with metabolic and physiological processes, thus exacerbating ecotoxicological stress exerted on terrestrial and aquatic ecosystems.

Lead is a hazardous heavy metal of considerable global concern as its exposure to humans has implications for neurological, developmental, and cardiovascular disorders. In numerous developing regions, wastewater treatment

[a]*Environmental Science and Industrial Development Department, Faculty of Postgraduate Studies for Advanced Sciences, Beni-Suef University, Egypt*

[b]*Interdisciplinary Centre for Water Research (ICWaR), Indian Institute of Science, Bengaluru, Karnataka 560012, India. E-mail: praveen@iisc.ac.in*

† Equal contribution.

infrastructure is either inadequate or ineffective. In these regions, lead originating from industrial effluents, mining activities, and deteriorating plumbing systems is commonly detected in surface waters. Conventional remediation strategies for lead-contaminated water encompass physicochemical techniques, such as precipitation, ion exchange, adsorption, and membrane filtration, along with biologically mediated methods. These conventional methods for remediation of lead are often expensive, energy-intensive, and inadequate for complete removal. As a result, nanoscale materials are being explored as alternative catalysts due to their high surface area, improved stability, and higher adsorption capacity, in contrast to their bulk counterparts. Metal-based nanoparticles synthesized by physical, chemical, or biological methods present significant potential for the remediation of lead. However, conventional synthesis has its own constraints, such as high cost, significant energy demand, and environmental issues. On the other hand, green syntheses employing biological systems, such as plants, fungi, or bacteria, serve as a more sustainable and viable approach.

Among the diverse nanoparticle synthesis strategies, plant-mediated green synthesis has gained significant attention as a prominent approach that could overcome the economic, environmental, and technical limitations of conventional physical and chemical approaches. The plant-mediated green synthesis approach utilizes phytochemicals present in the extracts of plants that simultaneously function as reducing, capping, and stabilizing agents to facilitate the formation of nanoparticles in an environmentally friendly and sustainable manner. This approach is economically viable, faster, and more suitable for large-scale production due to the ready availability of plant biomass. In this context, *Haldina cordifolia* has been investigated as a potential bioresource for nanoparticle synthesis, with its secondary metabolites facilitating the reduction and stabilization processes. Previous studies using different plants, such as *Jatropha curcas*[7] and *Garcinia mangostana*,[8] have successfully demonstrated the feasibility of synthesizing copper oxide nanoparticles (CuO NPs) *via* extract-based approaches. These findings collectively highlight that plant-assisted synthesis not only ensures simplicity and economic viability, but also promotes the environmentally friendly production of nanomaterials.

In the current study, CuO NPs were synthesized using an aqueous extract of *Haldina cordifolia* as a biogenic reducing and stabilizing agent. The synthesized NPs were characterized by analytical techniques such as UV-Vis, FTIR, XRD, TEM, SEM, TGA, and DLS analyses, to determine their structural and morphological characteristics. The functional efficacy of the CuO NPs was further assessed for their ability to remove lead ions from aqueous systems. Optimization studies were carried out by varying operational parameters such as temperature, pH, nanoparticle dosage, initial metal ion concentration, and contact time. To the best of our knowledge, this is the first-study detailing CuO NPs biosynthesis using *Haldina cordifolia* plant extract and its application in lead remediation. This green approach of applying biomass as a sustainable route aligns with the principles of the circular economy.

2 Methodology

2.1 Materials

Dried leaves of *Haldina cordifolia* served as the biological source material in this work. Copper acetate monohydrate (≥99% purity) was utilized as the precursor, while pH adjustments were carried out using 0.1 M NaOH (≥98%) and 0.1 M HCl (36–38%). Deionized water was employed throughout the study for the preparation of plant extracts and all standard solutions. Various concentrations of lead nitrate [$Pb(NO_3)_2$] (≥99% purity) were prepared, and 70% nitric acid (HNO_3, 70%, analytical grade) was used where necessary. All the reagents applied in the experimental procedures were of analytical grade.

2.2 Synthesis of liquid extract

The aqueous extract of *Haldina cordifolia* was prepared by following a previously reported protocol with minor modifications.[3] In brief, 10 g of the plant material in powdered form was mixed with 100 mL of distilled water and heated for 45 min at 50 °C with continuous stirring. The resultant solution was filtered using Whatman no. 1 filter paper to obtain a clear extract, which served as the bio-reducing medium for the synthesis of CuO NPs.

2.3 Green synthesis of HC-CuO NPs using *Haldina cordifolia* leaf extract

For the nanoparticle synthesis, 10 mL of *Haldina cordifolia* leaf extract was mixed with 80 mL of 1 mM copper acetate solution. The pH of the reaction mixture was adjusted to neutrality (pH ~7) using 0.1 M NaOH, after which the solution was maintained at 80 °C with continuous heating for 2 h in a 250 mL beaker. A discernible colour change from green to deep brown acted as a preliminary indication of CuO NPs formation. The precipitated material after natural cooling to ambient temperature was separated by centrifugation and repeatedly washed with distilled water to remove residual impurities. The obtained fraction was subjected to overnight oven drying at 80 °C, followed by calcination at 400 °C for 2 h to obtain crystalline CuO NPs.

2.4 Material characterization

The synthesized CuO NPs were characterized using a comprehensive set of analytical techniques to gain insights into the variation of physicochemical and structural characteristics of the synthesized CuO NPs before and after Pb(II) adsorption. The characterization techniques employed include Raman spectroscopy, Brunauer–Emmett–Teller (BET), surface area analysis, X-ray diffraction (XRD), ultraviolet-visible (UV-Vis) spectroscopy, thermogravimetric analysis (TGA), scanning electron microscopy (SEM) coupled with energy-dispersive X-ray spectroscopy (EDX), Fourier-transform infrared (FTIR) spectroscopy, and X-ray photoelectron spectroscopy (XPS). For Raman measurements, nanoparticle powders were examined in back-scattering mode using a confocal Raman spectrometer (Model STR-300, Seki Technotron Corp., Japan). Spectra were acquired

in the range of 100–1850 cm^{-1} under excitation with a 785 nm diode laser, employing a 50× objective lens. Scattered light was dispersed with a 600 lines/mm grating and detected using a CCD system. Each spectrum was recorded with twelve scans of 12 s exposure time, and baseline corrections were performed using GRAMS/AI software. Crystal data were obtained by XRD analysis with a Bruker D8 diffractometer, with scans performed between 3° and 70° (2θ) at a sweep rate of 4° min^{-1}. FTIR spectra were collected in ATR mode (Bruker Tensor) at 10 kHz to identify functional groups associated with nanoparticle stabilization. Optical properties were evaluated using a PerkinElmer Lambda 35 spectrophotometer over the wavelength range of 200–800 nm. The morphological and compositional analyses were conducted before and after Pb(II) adsorption using field-emission SEM (Zeiss ULTRA 55) integrated with EDX. Surface elemental states and binding energy profiles were examined by XPS (Thermo K-Alpha, Al anode). BET surface area and TGA analyses further complemented the structural and thermal characteristics. BET analysis was carried out using a BELSORP MAX-2 instrument (Microtrac MRB). The samples were degassed at 150 °C for 8 h prior to measurement.

2.5 Molecular docking simulations

Molecular docking simulations were conducted in order to predict potential interactions in the CuO and $Pb(NO_3)_2$ system. The 3D-structure data files (SDF) of CuO and $Pb(NO_3)_2$ were downloaded from the NIST Standard Reference Database (Data from NIST Standard Reference Database 69: NIST Chemistry WebBook, website used: https://webbook.nist.gov/chemistry/). The downloaded files were auto-optimized using Avogadro software (v1.2.0)[9] and subsequently saved as a PDB file. Blind docking was performed using AutoDock Tools (v1.5.7)[10] employing a grid box of 20 × 20 × 20 points with 0.375 spacing for AutoGrid, and a genetic algorithm was utilized as a search parameter for running AutoDock with 500 runs. CuO was assigned as the ligand, and $Pb(NO_3)_2$ was assigned as the macromolecule for docking. Additional parameters for Pb(II) and Cu atoms were added to the AD4_parameters.dat file to ensure successful docking.

3 Results

3.1 Molecular docking

The topmost docked conformation (ranked by energy) obtained in the molecular docking simulations had a binding energy of −0.36 kcal mol^{-1}. The negative binding energy obtained suggests a favourable affinity of CuO towards $Pb(NO_3)_2$. Furthermore, the anticipated interactions, as illustrated by Mol* 3D viewer,[11,12] reveal that metal coordination is the key interaction mechanism, as depicted in Fig. 1.

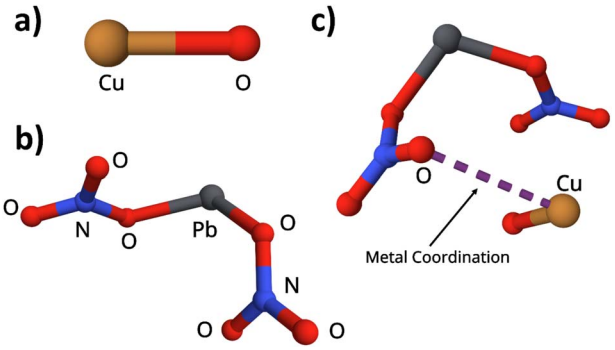

Fig. 1 Input structures of (a) CuO and (b) $Pb(NO_3)_2$ used for molecular docking (PDB files), and (c) topmost conformation (ranked by energy) obtained using molecular docking.

3.2 Characterization of CuO NPs

3.2.1 XRD measurements. P-XRD patterns of the green synthesized CuO NPs before and after Pb adsorption are presented in Fig. 2a. The XRD pattern of the CuO NPs shows distinctive peaks at 2Θ = 35.55°, 38.54°, 48.83°, 53.33°, 57.95°, 61.81°, 66.05°, 67.98°, and 75.18°, which correspond to the indexed planes (11−1), (111), (−202), (020), (202), (−113), (022), (113) and (004), respectively. The PXRD data for the CuO NPs are identical to those of the pure single-phase of CuO, which match well with JCPDF card number 01-072-0629, with $\beta = 99.54°$, $\alpha = \gamma = 90.00°$, a = 4.6837 Å, b = 3.4226 Å, and c = 5.1288 Å. The absence of any other peak confirms the purity of the developed CuO NPs. The average crystallite size of the developed CuO NPs was estimated using the two dominant peaks at (11−1) and (111) by applying the Scherer equation ($D = 0.9\ \lambda/\beta \cos\theta$, where λ represents the wavelength of X-ray radiation and β is the full width at half maximum of the peaks at the diffracting angle θ[13]). The calculated average crystallite size was 6.22 nm, indicating its nanocrystalline nature. The XRD pattern of the CuO after Pb(II) adsorption shows no significant change in the positions of the peaks, while the intensity of all the peaks increased, suggesting that the adsorption of the heavy metal increased the intensity of the peaks, and the higher the adsorption capacity, the higher the intensity, which agrees with the literature.[14]

3.2.2 FTIR analysis. The FT-IR spectrum of the developed CuO NPs (Fig. 2b) reveals significant peaks at 594, 475 and 678 cm^{-1},[15] corresponding to the characteristic vibrational frequencies of Cu(II)–O.[16–18] The carboxyl frequency peak is indicated at 1564 cm^{-1}, accompanied by a weak shoulder at 1662 cm^{-1}. The intensity of this band decreased after adsorption of Pb(II), suggesting the involvement of this bond in Pb(II) adsorption. The band observed at 1027 cm^{-1}, accompanied by a shoulder at 1096 cm^{-1}, corresponds to –OH bending and may also refer to C–O stretching.[19] The bands at 1411 and 2920 cm^{-1} conform to the stretching frequency of the C–H bond.[19] The intensities of both bands decreased after Pb(II) adsorption, suggesting the contribution of a C–H bond in the interaction between the CuO NPs and Pb(II).[20] The bands at about 2350 cm^{-1} indicate the presence of C═O stretching of alkanes.[21] There is a broad band located around 3345 cm^{-1} that is attributed to –OH groups of adsorbed water and/or plant-derived compounds (phenols and alcohols). After adsorption of Pb(II), the intensity of this band decreased, suggesting the involvement of hydrogen bonds in the adsorption of Pb, further supporting their role in the complexation with Pb(II). For the FT-

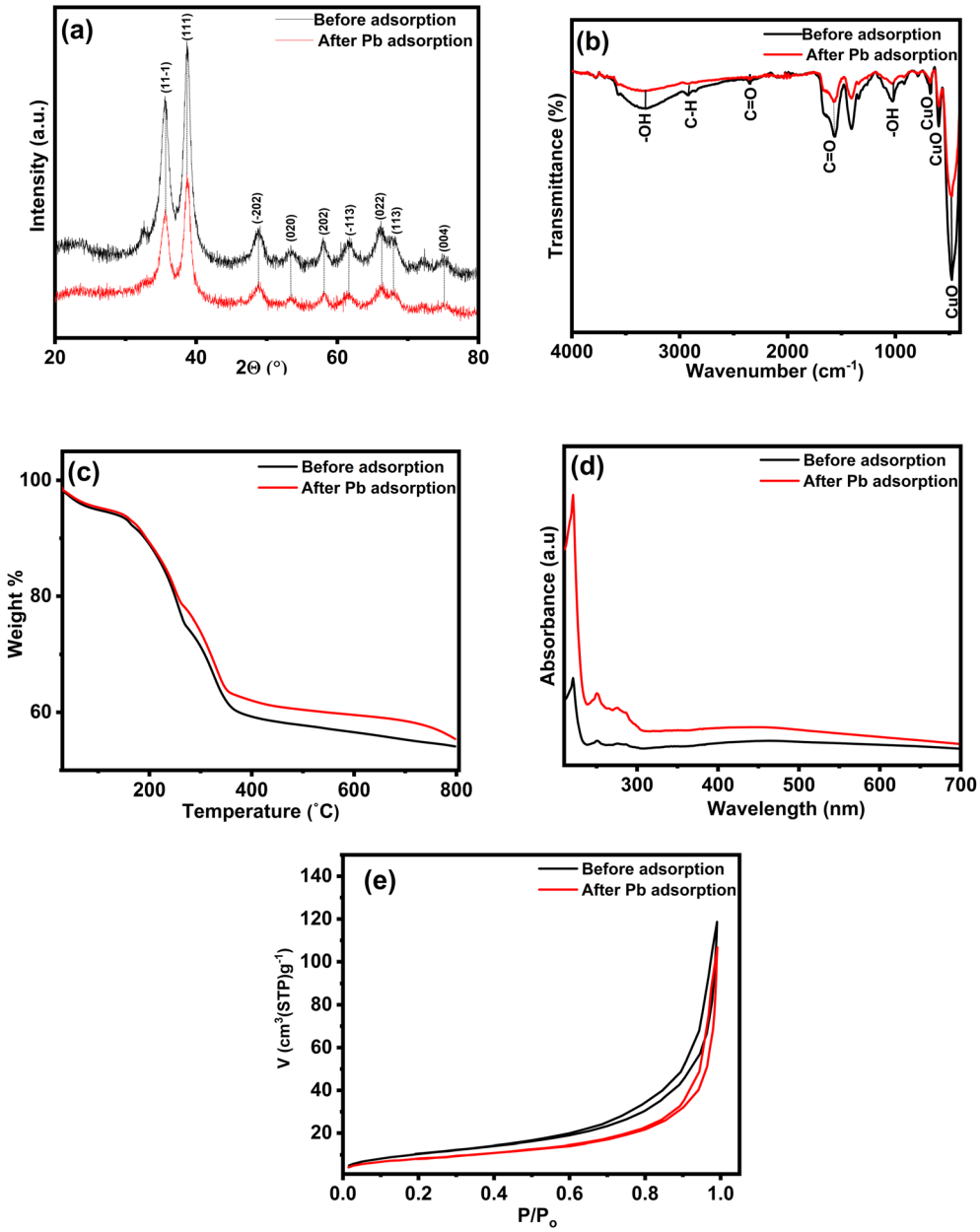

Fig. 2 XRD patterns (a), FTIR spectra (b), TGA profiles (c), UV-VIS spectra (d), and N_2 adsorption–desorption isotherms (e) of the CuO NPs before and after Pb(II) adsorption.

IR spectrum of CuO NPs after Pb(II) adsorption, the bands at 1027 and 475 cm^{-1} may refer to Pb–O, which confirms the adsorption of Pb(II) onto CuO NPs.[22,23] The above results are consistent with previous work on the adsorption of Pb(II) onto different adsorbents.[24]

3.2.3 Thermogravimetric analysis (TGA). The thermal profile of CuO NPs (Fig. 2c) reveals that a clear weight loss (5%) occurs in the region from 30 °C to 109 °C because of the elimination of the surface-adsorbed water. A major weight loss (34%) that begins at 153 °C and ends at 405 °C is attributed to the elimination of structural hydroxyl groups and decomposition of the organic component.[25] Increasing the temperature does not yield a significant change in the weight, suggesting that the residue is CuO NPs (54%). After adsorption of Pb, the thermal profile of CuO NPs (Fig. 2c) shows that there is no considerable shift in the decomposition temperature, while there is a decrease in the weight loss of the material after adsorption (by 3% beginning at 358 °C), suggesting that the attachment of Pb(II) improves the thermal stability of the CuO NPs.

3.2.4 UV spectroscopy. CuO NPs were developed *via* the reduction of copper acetate using complexes developed from the phytochemicals in *Haldina cordifolia* leaf extract. Subsequently, UV-VIS spectroscopy was used to detect the color of the solutions in the range 200–700 nm (Fig. 2d). Fig. 1e shows the distinctive peaks at 220, 250 and 280 nm attributed to surface plasmon

resonance (the free electrons repulsion onto the surface of NPs, with light variation at characteristic wavelengths), which confirm the development of the CuO NPs.[26,27] However, numerous parameters, such as crystallite size and shape, aggregation, and the initial concentration of the metal precursor, can impact the SPR.[28,29] Additionally, there is a broad peak around 450 nm that refers to the optical band gap.[30] After adsorption of Pb(II), the intensity of these significant peaks increased, which may be due to the involvement of these complexes in the uptake of Pb(II). Moreover, there is a shift and increase in the band at 279 after Pb(II) adsorption, compared to that of CuO NPs, which indicates a $\pi \rightarrow \pi^*$ transit of sp^2-hybridized C=C aromatic chains. The C=C functionalities arise from the polyphenols present in the plant extract.[31] This observation suggests that this bond is involved in the adsorption of Pb.

3.2.5 Surface area and pore analysis. The specific surface area (SSA) of the CuO NPs was determined by N_2 adsorption–desorption isotherms (Fig. 2e). The SSA of the CuO NPs decreased from 40.062 $m^2\ g^{-1}$ before adsorption to 29.948 $m^2\ g^{-1}$ after adsorption, combined with a reduction in the pore volume from 0.1793 to 0.1575 $cm^3\ g^{-1}$. The appearance of a hysteresis at high N_2 partial pressure adsorption/desorption isotherms for the CuO NPs before and after Pb(II) adsorption suggests that both isotherms are of type IV, referring to the interparticle space between the agglomerated CuO NPs.[32] There is no change in the hysteresis after adsorption, combined with the presence of agglomeration before as well as after adsorption, indicating the role of this interparticle space in the adsorption of Pb(II).

3.3 XPS characterization

The Cu 2p core-level spectrum (Fig. 3a) shows two peaks at 934.24 eV and 954.3 eV, which are attributed to Cu $2p^{3/2}$ and Cu $2p_{1/2}$, respectively, along with two satellite peaks at 943.01 eV and 962.9 eV. These two satellite peaks correspond to the spin–orbit levels of Cu $2p_{3/2}$ and Cu $2p_{1/2}$ (Fig. 3a) and arise from the ejection of photoelectrons from the core level that interact with electrons in the valence band. This transition results in the excitation of these electrons to a higher energy level, which leads to the formation of secondary peaks at higher energy than the basic peaks.[33] The disparity in the binding energies of the basic peaks and the secondary peaks is 20.06 and 19.89 eV, respectively, which aligns with the standard for CuO. After Pb(II) adsorption, the previous four peaks shifted from 934.24, 943.01, 954.3, and 962.9 eV to 934.36, 943.02, 954.45 and 963.02 eV, respectively (Fig. 3b). This change toward higher binding energy in the spectrum of Cu 2p after Pb(II) adsorption may be attributed to the interaction with Pb ions. In the O 1s spectrum, the peak shifts from 532.59 eV before adsorption (Fig. 3c) to 532.69 eV after adsorption (Fig. 3d) due to the interaction of oxygen-containing groups with Pb(II). Fig. 3e shows that Pb 4f peaks appear in the 137–144 eV range. By deconvolution of the peaks, two peaks are identified that are attributed to Pb $4f_{7/2}$ (139.05 eV) and Pb $4f_{5/2}$ (~143.97 eV), confirming successful Pb(II) adsorption onto the Cu NPs.[34]

3.3.1 SEM-EDX analysis. The developed CuO NPs have polygonal structures and were mostly spherical in shape with aggregates (Fig. 4a). This aggregation may be due to the surface functional capping by different phytochemicals present in the prepared extracts.[27] After adsorption of Pb(II) (Fig. 4b), significant holes are observed on the surface of the CuO NPs, suggesting that there is an ion exchange and/or chemical interaction between the CuO NPs and the Pb(II) ions. The EDS analysis shows that the CuO NPs (Fig. 4c) exhibit atomic percentages for Cu and O of 37.86% and 25.34%, respectively, in addition to a high carbon percentage (37.86%), which confirms the presence of functional groups on the CuO NPs. After Pb(II) adsorption (Fig. 4d), the weight percentage of Cu increased to 41.63%, and the carbon content decreased to 27.39% combined with the appearance of Pb(II) (6.52%). This signifies the active participation by the surface functional groups derived from the extract in the Pb(II) adsorption. The particle size distribution of the developed CuO NPs was assessed based on the SEM images using ImageJ software, which was developed by the National Institute of Health, USA. Fig. 4e shows that the average particle size distribution of the particles is 16 nm, with a standard deviation of 3.31 nm. However, very few discrete particles were analysed due to the extensive agglomeration of CuO NPs. Nevertheless, the particle size of the CuO NPs is larger than that calculated from the XRD data. This is attributed to the XRD calculations being based on crystalline size, while SEM images show the particle size.

3.4 Surface charge and adsorptive behaviour under different pH conditions

The point of zero charge (PZC) of HC-CuO NPs is reported to be around 2.07 (Fig. 5a), which governs their surface charge behavior in aqueous media. At pH values below this threshold, the nanoparticle surface is protonated, carrying a net positive charge, whereas at higher pH values it becomes negatively charged due to deprotonation of surface hydroxyl groups. This charge reversal has a direct influence on the adsorption of Pb(II) ions. Experimental studies conducted within the pH range of 2–7 demonstrated a strong pH-dependent adsorption, and the highest Pb(II) removal was recorded at pH 6. At pH 6, a removal efficiency of nearly 96.74% was achieved, whereas a marked reduction in adsorption was observed for pH values below 6. This reduction is due to surface protonation, which decreases the number of available negatively charged adsorption sites. This ultimately increases the competition between Pb^{2+} ions and protons for active binding sites. Moreover, the elevated concentration of H^+ ions at low pH suppresses Pb(II) uptake. Furthermore, a steady increase in adsorption was observed with increasing pH from 2 to 6 (Fig. 5b), ascribed to gradual surface deprotonation along with the coexistence of hydrolysed Pb species such as $Pb(OH)^+$ and $Pb^2(OH)_3^+$, which bind efficiently with the negatively charged surface groups. However, when the pH surpasses 6, the adsorption capacity again decreases. This behaviour is elucidated by the hydrolysis of Pb(II) followed by precipitation as $Pb(OH)_2$, which eventually decreases the concentration of dissolved Pb species available for adsorption. This is attributed to the rapid formation of $Pb(OH)_2$ precipitates

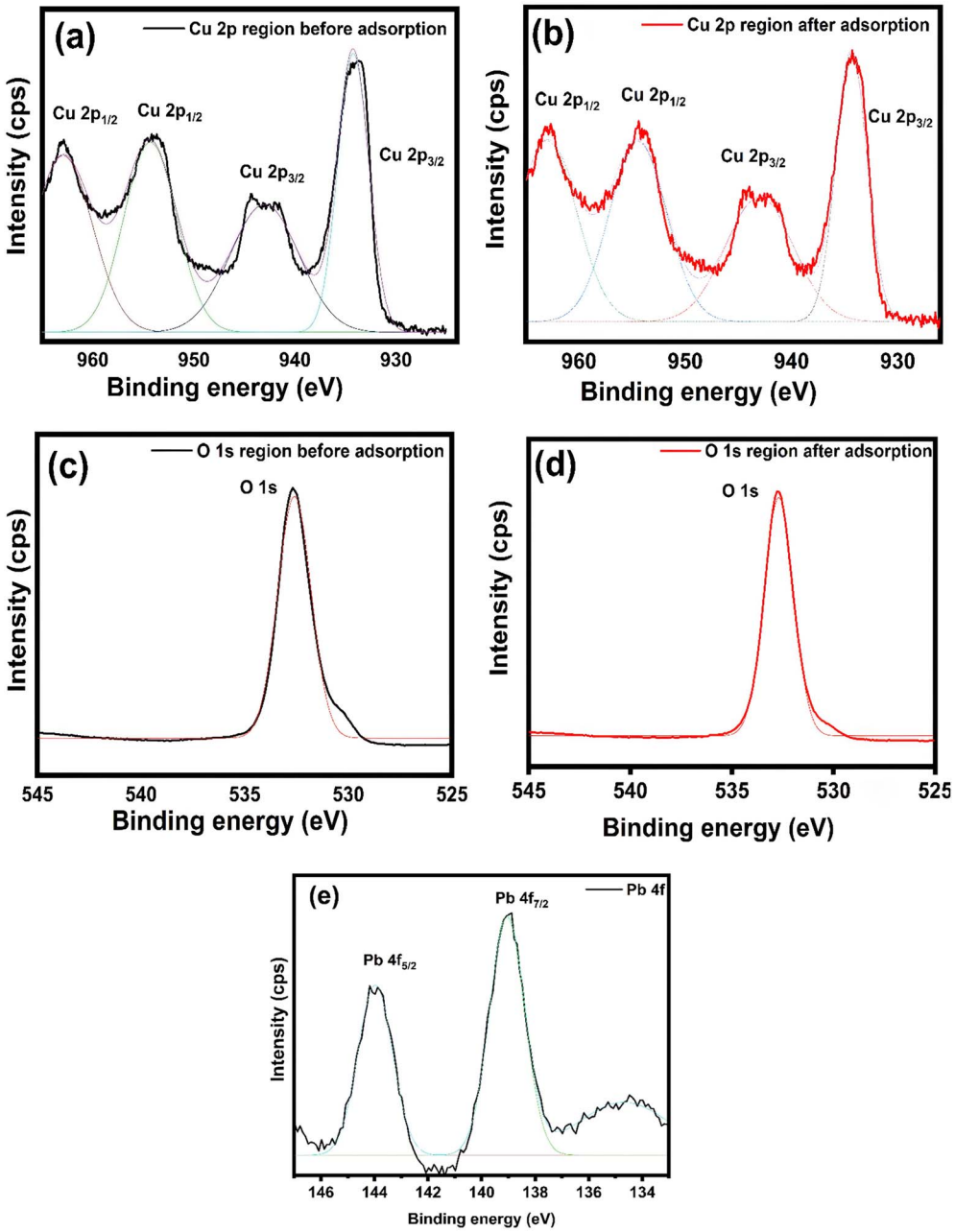

Fig. 3 XPS survey spectra: Cu 2p of CuO NPs before (a) and after (b) Pb(II) adsorption; O 1s of the CuO NPs before (c) and after (d) Pb adsorption; and Pb 4f (e) of the CuO NPs after Pb(II) adsorption (e).

that can cover the adsorbent surface due to site occupation or site competition, subsequently limiting access of Pb(II) to the internal pores or remaining active binding sites. Additionally, abundant hydroxide ions at alkaline pH compete with Pb(II) for surface sites and hence reduce the uptake. These cumulative factors restrict the removal efficiency above the optimal pH. Overall, the results clearly reveal that pH 6 is the most favourable condition for Pb(II) adsorption by HC-CuO NPs, providing an optimal balance between surface charge properties, metal ion speciation, and the availability of active binding sites.

3.5 Effect of dosage of CuO-NPs

The effect of HC-CuO NPs dosage on Pb(II) removal was evaluated by varying the adsorbent concentration from 10 to 50 mg L^{-1} (Fig. 5c). The results revealed consistently high removal efficiencies for all tested dosages, with percentage values varying from 97.65% at 10 mg L^{-1} to 98.91% at 50 mg L^{-1}. The overall efficiency showed a modest increase with dosage and relatively marginal variation, which suggests that Pb(II) removal continues to be highly effective even at low adsorbent concentrations. Specifically, efficiencies of 98.17%, 98.39%, and 98.67% were attained at 20, 30, and 40 mg L^{-1} dosages, respectively, before reaching the maximum of 98.91%

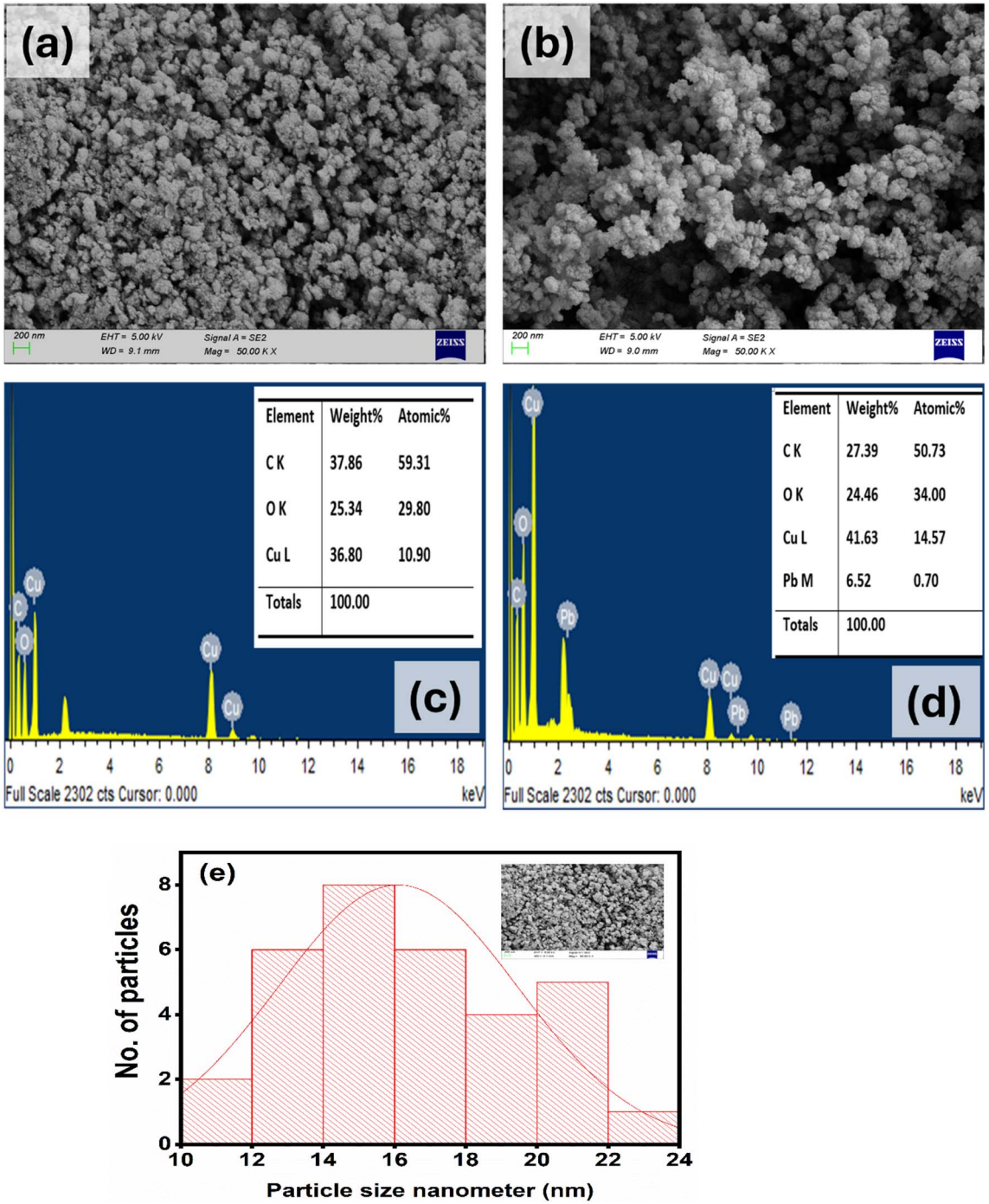

Fig. 4 SEM micrographs of the CuO NPs before (a) and after (b) Pb(II) adsorption, EDX spectra of the CuO NPs before (c) and after (d) Pb(II) adsorption and particle size distribution histogram of CuO NPs produced using ImageJ and Origin software (e).

at 50 mg L^{-1}. The near-saturation of adsorption efficacy within this dosage range implies that HC-CuO NPs have a strong inherent affinity for Pb(II) ions. Thus, high efficiency at low dosages could be due to the high density of active binding sites relative to the Pb(II) concentration in solution. However, with increasing dosage, aggregation of NPs may occur that effectively reduces the surface area per unit mass, resulting in minimal incremental enhancements in removal efficiency. This phenomenon indicates that, beyond a threshold dosage, further addition of NPs does not significantly contribute to overall uptake because the available Pb(II) ions have already been effectively captured. The synergy of high removal efficiency at all dosages and short equilibrium time confirms the efficiency of HC-CuO NPs as an adsorbent. Notably, even at dosages as low as 10 mg L^{-1}, Pb(II) removal exceeded 97%, underlining their suitability for practical applications with minimal material

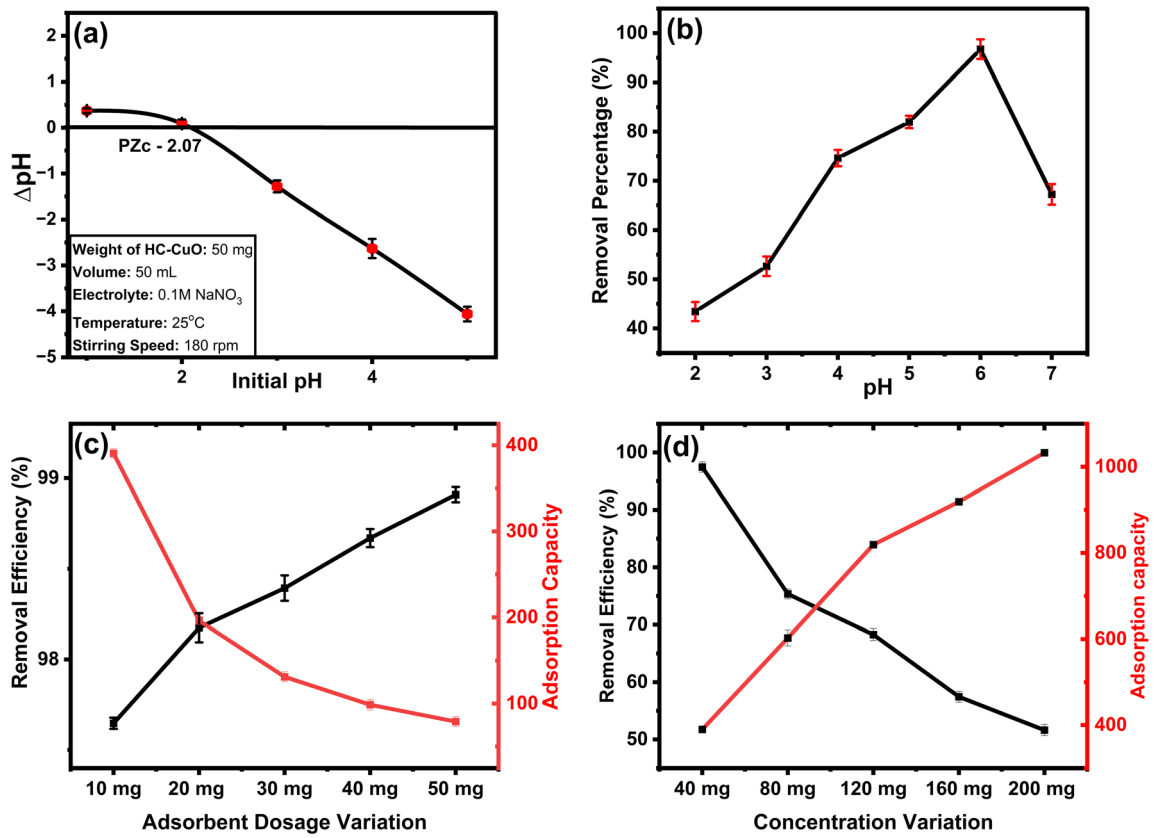

Fig. 5 Zeta potential charge variation with the initial pH for the CuO NPs (a) and effect of pH (b), adsorbent dose (c), and initial Pb(II) concentration (d) on the adsorption of Pb(II) onto the CuO NPs.

consumption. Overall, the data confirm that HC-CuO NPs demonstrate excellent Pb(II) adsorption efficiency, with optimal performance at a concentration of 50 mg L^{-1}.

3.6 Effect of Pb(II) concentration

Fig. 5d illustrates the relationship between the initial Pb(II) concentration and the adsorption capacity of HC-CuO nanoparticles. A strong dependence between the adsorption performance and the initial concentration of Pb(II) ions was observed. Thus, an increase in the initial concentration from 40 mg L^{-1} to 200 mg L^{-1} significantly increased the adsorption capacity from 389.78 mg g^{-1} to 1032.57 mg g^{-1}. This convincing increase in capacity with increasing concentration underlines the strong affinity of HC-CuO NPs for Pb(II) ions and demonstrates the impact of concentration gradient on mass transfer processes. At low Pb(II) concentrations, the adsorption sites on the surface of nanoparticles remain unsaturated, allowing effective binding by nearly all the available ions. Thus, adsorption capacity increases swiftly with the increase in concentration because of heightened collision frequency between Pb(II) ions and the active sites on the HC-CuO surfaces. This stage demonstrates the occurrence of favourable electrostatic interactions and efficient utilization of active surface binding domains. However, as the concentration increases further and a substantial portion of the active sites becomes occupied, the rate of increase in the adsorption capacity slows down. Eventually, this results in a decrease in the removal percentage. Moreover, due to the progressive saturation of the active binding sites, the adsorption capacity starts to increase in a non-linear manner at higher concentrations. Hence, the observed behaviour can be attributed to three main factors: (i) the driving force for mass transfer improves as Pb(II) concentration increases, (ii) greater ionic abundance enhances the probability of successful interactions with the nanoparticle surface, and (iii) the finite number of binding sites eventually imposes a saturation limit, beyond which further increases in concentration contribute minimally to adsorption. These findings confirm that HC-CuO NPs possess a high affinity and capacity for Pb(II), but their performance is ultimately constrained by the saturation of surface adsorption sites at elevated concentrations.

3.7 Kinetic studies

Fig. 6a–e compare the kinetics models of Pb(II) adsorption onto CuO NPs when fitting experimental data with non-linear models. To compare the applicability of each model, we determined the coefficient of determination (R^2) and normalized standard deviation Δq (%) according to eqn (1) and (2), respectively.

$$R^2 = \frac{\sum \left(q_{t,\mathrm{cal}} - \overline{q}_{t,\mathrm{exp}}\right)^2}{\sum \left(q_{t,\mathrm{cat}} - \overline{q}_{t,\mathrm{exp}}\right)^2 + \sum \left(q_{t,\mathrm{cal}} - \overline{q}_{t,\mathrm{exp}}\right)^2} \quad (1)$$

$$\Delta q(\%) = 100 \times \sqrt{\frac{\left[\left(q_{t,\mathrm{exp}} - q_{t,\mathrm{cal}}\right)/q_{t,\mathrm{exp}}\right]^2}{(n-1)}} \quad (2)$$

Based on the adsorption kinetics of Pb(II) onto CuO NPs, the experimental data were fitted using PFO, PSO, MFSO, Avrami and IPD models (Fig. 6a–e); the corresponding degree of fitting values are reported in Table 1.

The P1O model (Fig. 6a) is suitable for effectively characterizing the Pb@CuO NPs across all concentrations under study with high R^2 values (0.990, 0.996, 0.996, 0.989 and 0.965 for initial Pb(II) concentrations of 40, 80, 120, 160 and 200 mg L^{-1}, respectively). Comparing the values of R^2 and Δq (%) along with fitting results displayed in Fig. 6a, the P1O model exhibits higher accuracy at low concentrations, and it describes the adsorption system under study better at concentrations of 40 mg L^{-1} than at 200 mg L^{-1}. This is also confirmed with the values of Δq(%), which increased with increasing initial Pb(II) concentrations. Moreover, the agreement between the experimental and calculated data is stronger at lower (40 mg L^{-1}) than at higher (200 mg L^{-1}) concentrations. Fig. 6b presents the fitting of the P2O model to the experimental values of Pb(II) adsorption onto CuO NPs. This model adequately represents the adsorption system within a defined range of initial Pb concentrations. For instance, at low concentration (40 mg L^{-1}), the predicted q_e (529.82 mg g^{-1}) was notably higher than the experimental value (389.78 mg g^{-1}), as indicated by the higher value of Δq (%). Moreover, at high Pb(II) concentration

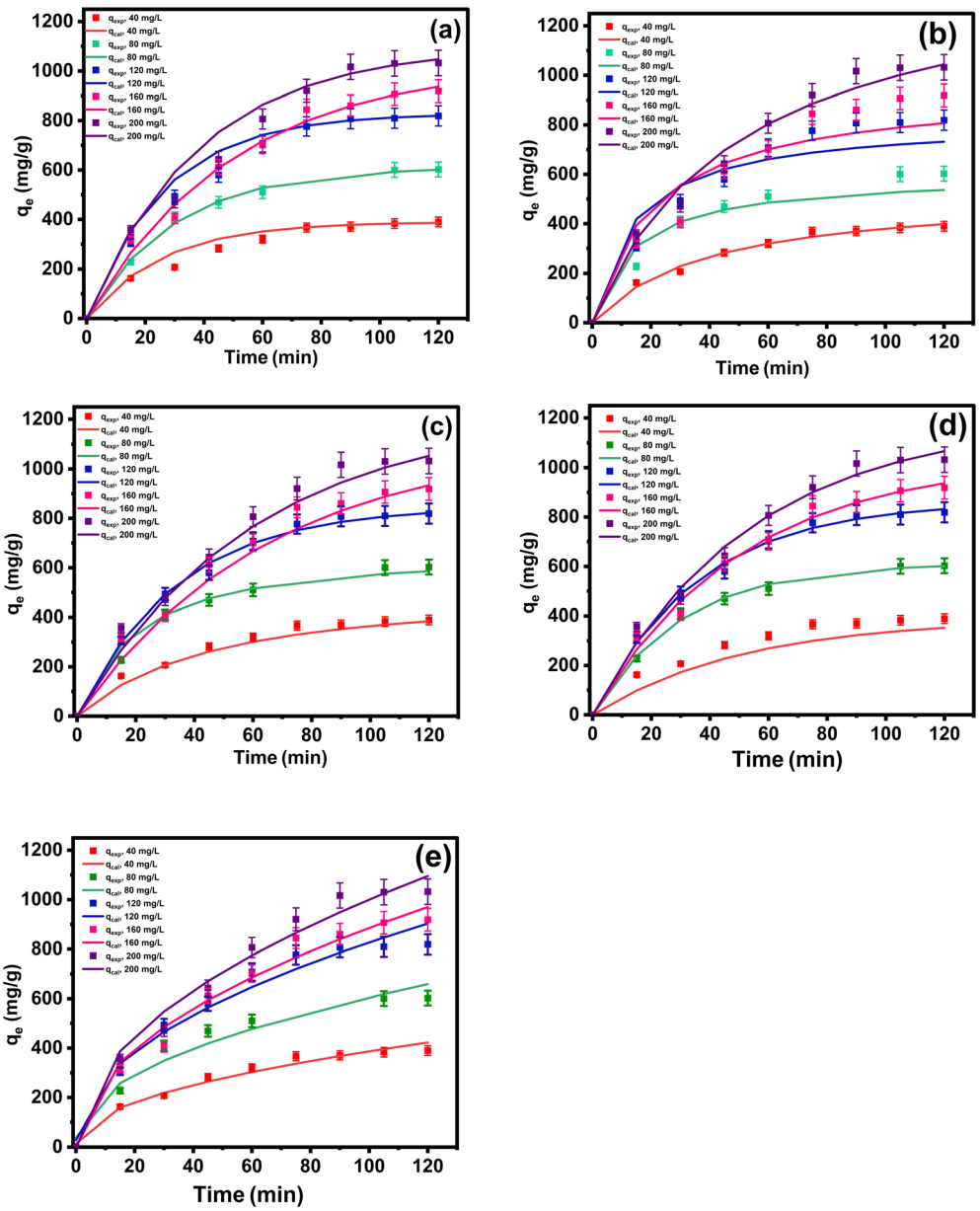

Fig. 6 Fitting of the experimental data with PFO (a), PSO (b), MFSO (c), Avrami (d) and IPD (e) models for the array of results for Pb(II) adsorption onto CuO NPs at initial Pb(II) concentrations of 40, 80, 120, 160 and 200 mg L^{-1}.

Table 1 Factors of the kinetic models for the adsorption of Pb(II) onto CuO NPs

ParameterModel	Parameter	Initial conc. C_o [mg L^{-1}]				
		40	80	120	160	200
P1O $q_t = q_e(1 - e^{-k_1 t})$	q_{exp} (mg g^{-1})	389.78	602.70	809.85	919.06	1032.58
	K_1 [min^{-1}]	0.0271	0.0330	0.0377	0.019	0.0258
	q_e [mg g^{-1}]	406.85	612.83	828.96	1033.37	1097.02
	R^2 [–]	0.990	0.996	0.996	0.989	0.965
	Δq (%)	0.475	1.26	2.55	1.98	2.74
P2O $q_t = \frac{q_e^2 K_2 t}{1 + q_e K_2 t}$	K_2 [g mg^{-1} min^{-1}]	4.78×10^{-5}	0.0001	8.47×10^{-5}	4.95×10^{-5}	4.95×10^{-5}
	q_e [mg g^{-1}]	529.82	600.00	820.00	950.00	1040
	R^2 [–]	0.991	0.942	0.915	0.907	0.885
	Δq (%)	13.50	4.96	5.11	5.42	2.14
MFSO $q_t = q_e \frac{1 - e^{(-Kt)}}{1 - f_2 e^{(-Kt)}}$	K [mg g^{-1} min^{-1}]	0.0153	0.0141	0.0292	0.0153	0.01647
	q_e [mg g^{-1}]	434.94	621.81	847.03	1112.15	1222.678
	f_2 [–]	0.4786	0.727	0	0	0.0005
	R^2 [–]	0.991	0.979	0.974	0.981	0.946
	Δq (%)	2.58	2.67	0.77	2.91	2.31
Avrami $q_t = q_e[1 - e^{(-k_{av} t)n_{av}}]$	q_e [mg g^{-1}]	406.85	612.89	862.69	1033.37	1191.77
	k_{av} [min^{-1}]	0.1693	0.1869	0.1717	0.1447	0.1411
	n_{av} [–]	0.1599	0.1766	0.1623	0.1368	0.1333
	R^2 [–]	0.990	0.996	0.996	0.989	0.989
	Δq (%)	6.72	1.26	0.90	1.98	2.04
IPD $q_t = K_{ip}\sqrt{t} + C_{ip}$	k_{ip} [mg g^{-1} $min^{1/2}$]	37.25	56.63	79.79	88.57	100.03
	C_{ip} [mg g^{-1}]	14.519	38.88	29.15	0.005	0.0005
	R^2 [–]	0.977	0.954	0.971	0.979	0.981
	Δq (%)	8.92	4.31	2.46	2.38	2.48

(200 mg L^{-1}), the correlation coefficient (R^2 = 0.885) was determined to be comparatively low. As illustrated in Fig. 6c, the MFSO model fails to adequately describe the adsorption behaviour of Pb(II) on CuO NPs, as the calculated values deviate from the experimental data. Even though the model yields high R^2 values (0.991, 0.979, 0.974, 0.981 and 0.946 for initial Pb(II) concentrations of 40, 80, 120, 160 and 200 mg L^{-1}, respectively). Whereas, as illustrated in Fig. 6d, Avrami model demonstrated the best fitting compared to the other models, as affirmed by the significant correlation between the calculated and the experimental values of Pb(II) adsorption onto CuO NPs up to an initial Pb(II) concentration of 120 mg L^{-1}. However, beyond this concentration, the model accuracy decreases as the predicted values of q_e (1033.37 and 1191.77 mg g^{-1} for initial Pb(II) concentrations of 160 and 200 mg L^{-1}, respectively) are higher than the experimental ones (919.06 and 1032.58 mg g^{-1} for initial Pb(II) concentrations of 160 and 200 mg L^{-1}, respectively). Even though the model yields high R^2 values (0.989 for both Pb(II) initial concentrations of 160 and 200 mg L^{-1}). In contrast to P1O, P2O, MFSO and Avrami models, the IPD model (Fig. 6e) fits the adsorption system Pb(II)@CuO NPs better at higher concentrations of Pb(II) rather than lower concentrations, where the values of k_{ip} increase with increasing initial Pb(II) concentration. Additionally, the R^2 values increased from 0.977 to 0.981 with increasing initial Pb(II) concentration from 40 to 200 mg L^{-1}. Thus, the kinetic results show that the initial Pb(II) concentration has an important impact on the kinetics of the adsorption of Pb(II) onto the CuO NPs.

Where q_t is the adsorption capacity of Pb(II) in mg g^{-1} at time t, C_{ip} (mg g^{-1}), k (mg g^{-1} min^{-1}), k_1 (min^{-1}), k_2 (g mg^{-1} min^{-1}), and k_{av} (min^{-1}) are the IPD, MFSO, P1O, P2O, and Avrami models constants, respectively, f_2 (–) and k_{ip} (mg g^{-1} $min^{-1(1/2)}$) are the MFSO and IPD coefficients, and n_{av} (–) is the Avrami component.

3.8 Adsorption isotherm modeling

The adsorption isotherms are crucial for investigating the mechanism and adsorption affinity of CuO NPs for Pb(II). Accordingly, eleven models, Langmuir, Freundlich, Langmuir–Freundlich, Sips, Toth, Redlich–Peterson, Dubinin–Radushkevich, Khan, Baudu, Fritz–Schlünder and Temkin, were adopted to fit the experimental data for Pb(II) adsorption onto CuO NPs at ambient temperature (298 K). As per the IUPAC classification of adsorption isotherms, the adsorption of Pb(II) onto CuO NPs followed the L-type isotherm, suggesting a strong interaction between the Pb(II) ions (adsorbate) and CuO NPs (adsorbent).[35] The Freundlich model (Fig. 7a) most accurately describes the Pb(II) adsorption behaviour on CuO NPs, showing a strong correlation between experimental and calculated data, as affirmed by the high correlation coefficient (R^2 = 0.959). In contrast, the alternative 2-parameter models, Langmuir, Temkin, and Dubinin–Radushkevich (Fig. 7a), failed to adequately describe the Pb(II) adsorption onto CuO NPs owing to the significant deviation between the experimental data and the calculated data, as reflected by their low R^2 values (Langmuir (R^2 = 0.702), Temkin (R^2 = 0.896) and Dubinin–Radushkevich (R^2 = 0.693)). Even though the 3-parameter models exhibited high R^2 values (Langmuir–Freundlich (R^2 = 0.958), Redlich Peterson (R^2 = 0.959), Khan (R^2 = 0.959), Toth (R^2 = 0.959), and Sips (R^2 =

0.959)), these models failed to accurately describe the adsorption of Pb(II) onto CuO NPs. This unsuitability arises from the substantial discrepancies between the calculated q_{max} values and the experimental value, which were overestimated by the Langmuir–Freundlich, Redlich Peterson, Toth, and Sips (Fig. 7b) and underestimated by the Khan model, as shown in Table 1. Moreover, the Baudu and Fritz–Schlünder models (Fig. 7c) are not suitable for the Pb(II)@CuO NPs adsorption system since the calculated values of q_{max} according to both models are much lower than the experimental value, despite the high R^2 (Baudu ($R^2 = 0.959$) and Fritz–Schlünder ($R^2 = 0.959$)). The adsorption capacity obtained in this study (1032.57 mg g^{-1}) is substantially higher than the values reported for CuO-based adsorbents in the literature, as tabulated in Table 3 (typically <200 mg g^{-1}), indicating a significantly enhanced Pb(II) uptake (Table 2).

Where C_e: equilibrium concentration of Pb(II) in solution; q_{max}: the maximum adsorption capacity (mg g^{-1}); K_L: Langmuir isotherm constant (L mg^{-1}); K_{LF}: affinity constant for heterogeneous solids; K_F (L mg^{-1}) and n: Freundlich constants corresponding to adsorption capacity and intensity, respectively; M_{LF}: heterogeneous parameter ($0 < M_{LF} < 1$); k_s: Sips isotherm constant; n_s: Sips isotherm exponent (referred to as heterogeneity factor); K_R and a_R: Redlich–Peterson constants; β_R: Redlich–Peterson model exponent ($0 < \beta_R < 1$); K_T (mg g^{-1}) and a_T (mg L^{-1}): Toth constants; Z: degree of heterogeneity of the adsorption systems; m_1, m_2, K_1, and K_2: Fritz–Schlünder parameters; and β: Temkin isotherm constant.

3.9 Adsorption mechanism

The SEM results (Fig. 4) suggest that Pb(II) ions interact chemically with CuO NPs, and that ion exchange is possible. FTIR results (Fig. 2) support the proposed mechanism in which there is an increment in the intensity of the bonds after adsorption. This suggests the involvement of complexation, precipitation, and ion exchange in the adsorption process. However, the interaction is driven by the development of complexation between Pb ions and the functional groups on the CuO NPs. These functional groups coordinate with Pb ions *via* their lone electron pairs.[41,42] Moreover, the results of pH studies (Fig. 5a and b) suggest the presence of electrostatic attraction between the cationic Pb species, such as $Pb(OH)^+$ and $Pb^2(OH)_3^+$, and the negatively charged surface groups on the CuO NPs. Ion exchange studies also support the attachment of Pb(II) ions onto the CuO NPs, where –OH groups play a significant role in exchanging Pb(II) with ions. The ion-exchange mechanism is supported by other observations in previous investigations.[43]

3.10 Reusability studies

Reusability studies were carried out in 0.25 M NaOH. A solution of Pb(II) with an initial concentration of 40 mg L^{-1} was

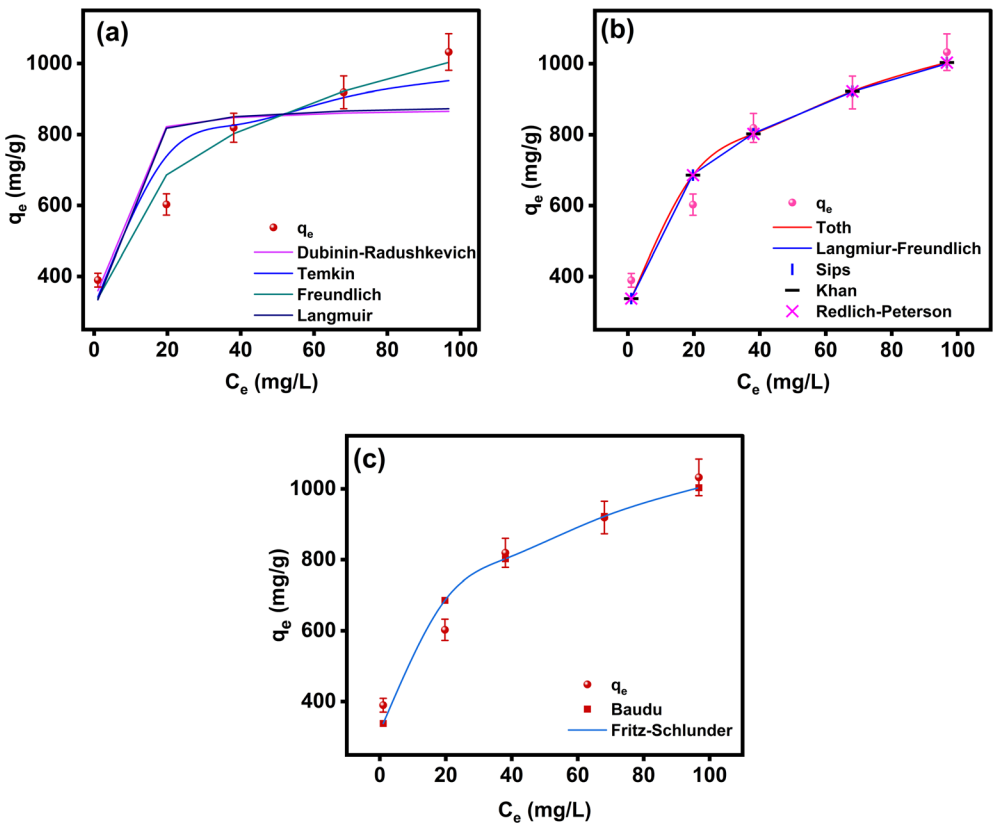

Fig. 7 Adsorption isotherm modelling for Pb(II) adsorption onto CuO NPs using: 2-parameter models; Langmuir, Freundlich, Temkin and Dubinin–Radushkevich (a); 3-parameter models: Langmuir–Freundlich, Redlich Peterson, Khan, Toth, and Sips (b); and 4- and 5-parameter models: Baudu and Fritz–Schlünder, respectively (c).

Table 2 The parameters of the adsorption isotherm modelling for the Pb(II) adsorption onto CuO NPs; 2-parameters models: Langmuir, Freundlich, Temkin and Dubinin–Radushkevich; 3-parameter models: Langmuir–Freundlich, Redlich Peterson, Khan, Toth, Sips and 4- and 5-parameter models: Baudu and Fritz–Schlünder, respectively

Model	Parameter	Value	Model	Parameter	Value
Langmuir $q_e = q_{max}\frac{K_L C_e}{1+K_L C_e}$	q_{max} (mg g^{-1})	888.49	Freundlich $q_e = KfC_e^{1/n}$	$1/n$ (–)	0.239
	K_L (L mg^{-1})	0.590		K_F (L mg^{-1})	336.36
	R^2 (–)	0.702		R^2 (–)	0.959
Temkin $q_e = \frac{RT}{b_T}\ln(A_T C_e)$	b_T (L g^{-1})	18.61	Dubinin–Radushkevich $q_e = q_m \exp(-k_{ad}\,\varepsilon^2)$	q_m (mg g^{-1})	877.43
	A_T	12.56		K_{ad}	0.0003
	R^2 (–)	0.896		R^2 (–)	0.693
Langmuir–Freundlich $q_e = \frac{q_{max}(K_{LF}C_e)^{M_{LF}}}{1+(K_{LF}C_e)^{M_{LF}}}$	q_{MLF} (mg g^{-1})	20 519	Sips $q_e = \frac{q_{max}K_s(C_e)^{1/n_s}}{1+K_s(C_e)^{1/n_s}}$	q_{max} (mg g^{-1})	3.06×10^6
	K_{LF} (L mg^{-1})	5.57×10^{-8}		K_s (L g^{-1})	0.0001
	M_{LF} (–)	0.2449		$1/n$	0.2391
	R^2 (–)	0.958		R^2 (–)	0.959
Redlich–Peterson $q_e = \frac{K_R C_e}{1+a_R C_e^{\beta R}}$	K_R (L g^{-1})	5.25×10^5	Toth $q_e = \frac{K_T C_e}{(a_T + C_e^Z)^{1/Z}}$	K_T (mg g^{-1})	6.16×10^5
	a_R ((L mg^{-1})$^\beta$)	1560		a_T (L mg^{-1})	2406.7
	β (–)	0.761		Z (–)	0.761
	R^2 (–)	0.959		R^2 (–)	0.959
Khan $q_e = \frac{q_{max}b_K C_e}{(1+b_K C_e)^{a_K}}$	q_{max} (mg g^{-1})	43.11	Fritz–Schlünder $q_e = \frac{q_{max}K_1 C_e^{m_1}}{1+K_2 C_e^{m_2}}$	q_{mFSS} (mg g^{-1})	120.28
	b_K	5369		K_1	2.83
	a_K	0.7609		K_2	0.0124
	R^2 (–)	0.959		m_1	0.239
Baudu $q_e = \frac{q_{max}\,\mathrm{bo}C_e^{1+x+y}}{1+\mathrm{bo}\,C_e^{1+x}}$	q_m (mg g^{-1})	336.35		m_2	0.002
	b_0 (–)	1.34×10^9		R^2 (–)	0.959
	x (–)	0.239			
	y (–)	0.003			
	R^2 (–)	0.959			

Table 3 Comparative studies for the adsorption of Pb(II) using CuO NPs

Material	Synthesis/adsorbent type	Pb(II) adsorption capacity (q_m, mg g^{-1})	References
CuO NPs	Green plant extract CuO NPs	~88.8 mg g^{-1} (CuO NP-1); ~82.8 mg g^{-1} (CuO NP-2)	36
CuO nanostructures	Microwave synthesis	~115–125 mg g^{-1} depending on morphology	37
Green CuO NPs	Eco-friendly green synthesis	~95% removal	38
CuO nanofibers (CuONFs)	Electrospun PAN/CuO nanofibers	~151.34 mg g^{-1}	39
CS/PVA/CuO composite	Chitosan/poly(vinyl alcohol)/CuO	~116.84 mg g^{-1}	40
CuO NPs	Green plant extract CuO NPs	1032.57 mg g^{-1}	Present

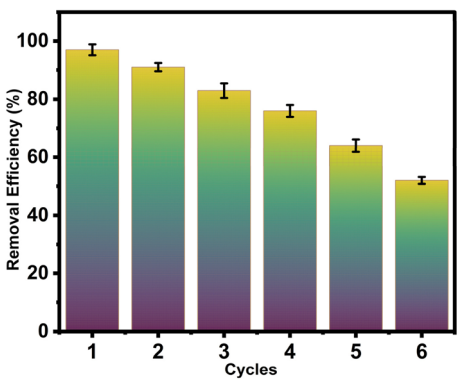

Fig. 8 Stability and reusability of CuO NPs after the Pb adsorption.

incubated in a shaker with 10 mg L^{-1} of the adsorbent in a rotatory agitator at 200 rpm and room temperature for 2 h. It was then filtered after adsorption, and the Pb concentration was determined. The dried material was washed with 0.25 M NaOH and reused in the next step. The regeneration rate was initially good in the first three cycles and dropped dramatically to 52.87% in the sixth cycle (Fig. 8). This confirms that the synthesized material can be reused in up to six cycles, making it a good regenerative material for Pb(II) adsorption.

4 Conclusion

To summarize, CuO NPs were synthesized using *Haldina cordifolia* for the removal of Pb(II) from water. The docking results demonstrated a binding energy of −0.36 kcal mol^{-1}, suggesting a strong adsorption efficiency between the CuO NPs and Pb(II) ions. Adsorption isotherm modelling identified the Freundlich isotherm as the best match with the experimental data, indicating heterogeneous multilayer adsorption. Both physical and chemical interactions were found to be involved in the adsorption mechanism. Moreover, adsorption kinetics revealed that pseudo-first-order, pseudo-second-order, Avrami, mixed first- and second-order, and intraparticle diffusion could describe the adsorption behaviour of Pb(II) on the CuO NPs.

However, the kinetics were strongly influenced by the initial Pb(II) concentration. Thus, further investigations are required that focus on the large-scale production of CuO NPs as well as the removal of multiple metals from real wastewater systems.

Conflicts of interest

There are no conflicts to declare.

Data availability

All relevant data supporting this research are included in the article.

Acknowledgements

S. S. acknowledges support from the DBT-RA program (Award No. DBT-RA/2022/July/N/2044). The authors acknowledge financial support from the MoE-STARS grant and thank ICWaR and IISc for laboratory and instrumentation facilities. Radhika Varshney would like to acknowledge MHRD for the Prime Minister's Research Fellowship (PMRF): TF/PMRF-22-5459.

References

1 Imminent risk of a global water crisis, warns the UN World Water, https://www.unesco.org/en/articles/imminent-risk-global-water-crisis-warns-un-world-water-development-report-2023, accessed 2 September 2025.
2 M. Naddaf, *The World Faces a Water Crisis, and 4 Powerful Charts Show How | Scientific American*, 2023.
3 D. M. Nzilu, E. S. Madivoli, D. S. Makhanu, S. I. Wanakai, G. K. Kiprono and P. G. Kareru, *Sci. Rep.*, 2023, **13**, 1–18.
4 S. Fang, C. Hua, J. Yang, F. Liu, L. Wang, D. Wu and L. Ren, *J. Hazard. Mater.*, 2025, **485**, 136812.
5 M. Adnan, B. Xiao, M. U. Ali, P. Xiao, P. Zhao, H. Wang and S. Bibi, *Ecotoxicol. Environ. Saf.*, 2024, **274**, 116189.
6 D. Piwowarska, E. Kiedrzyńska and K. Jaszczyszyn, *Crit. Rev. Environ. Sci. Technol.*, 2024, **54**, 1436–1458.
7 M. K. Ghosh, S. Sahu, I. Gupta and T. K. Ghorai, *RSC Adv.*, 2020, **10**, 22027–22035.
8 Y. Bin Chan, M. Aminuzzaman, Y. F. Win, S. Djearamane, L. S. Wong, S. K. Guha, H. Almohammadi, M. Akhtaruzzaman and L. H. Tey, *Catalysts*, 2024, **14**, 486.
9 M. D. Hanwell, D. E. Curtis, D. C. Lonie, T. Vandermeerschd, E. Zurek and G. R. Hutchison, *J. Cheminf.*, 2012, (4), 1–17.
10 G. M. Morris, H. Ruth, W. Lindstrom, M. F. Sanner, R. K. Belew, D. S. Goodsell and A. J. Olson, *J. Comput. Chem.*, 2009, **30**, 2785–2791.
11 H. M. Berman, J. Westbrook, Z. Feng, G. Gilliland, T. N. Bhat, H. Weissig, I. N. Shindyalov and P. E. Bourne, *Nucleic Acids Res.*, 2000, **28**, 235–242.
12 D. Sehnal, S. Bittrich, M. Deshpande, R. Svobodová, K. Berka, V. Bazgier, S. Velankar, S. K. Burley, J. Koča and A. S. Rose, *Nucleic Acids Res.*, 2021, **49**, W431–W437.
13 M. Verma, I. Tyagi, R. Chandra and V. K. Gupta, *J. Mol. Liq.*, 2017, **225**, 936–944.
14 S. R. Yasin, S. S. Jasim and I. A. Al-Baldawi, *Desalination Water Treat.*, 2025, **323**, 101345.
15 V. V. T. Padil and M. Černík, *Int. J. Nanomed.*, 2013, **8**, 889–898.
16 V. U. Siddiqui, A. Ansari, R. Chauhan and W. A. Siddiqi, *Mater Today Proc*, 2021, **36**, 751–755.
17 M. Vaseem, A. Umar, Y. B. Hahn, D. H. Kim, K. S. Lee, J. S. Jang and J. S. Lee, *Catal. Commun.*, 2008, **10**, 11–16.
18 C. Tamuly, I. Saikia, M. Hazarika and M. R. Das, *RSC Adv.*, 2014, **4**, 53229–53236.
19 K. Jyoti, M. Baunthiyal and A. Singh, *J. Radiat. Res. Appl. Sci.*, 2016, **9**, 217–227.
20 Y. S. Jara, E. T. Mohammed and T. T. Mekiso, *Next Mater.*, 2025, **8**, 100742.
21 P. P. N. V. Kumar, U. Shameem, P. Kollu, R. L. Kalyani and S. V. N. Pammi, *Bionanoscience*, 2015, **5**, 135–139.
22 S. Aryam Behera, D. Khatua, R. Kumar Singh, R. N. P. Choudhary and P. Ganga Raju Achary, *Inorg. Chem. Commun.*, 2024, **163**, 112370.
23 L. Wang, H. Zhou, J. Hu, B. Huang, M. Sun, B. Dong, G. Zheng, Y. Huang, Y. Chen, L. Li, Z. Xu, N. Li, Z. Liu, Q. Chen, L. D. Sun and C. H. Yan, *Science*, 2019, **363**, 265–270.
24 S. Zhang, J. Lan, L. Yu, Y. Luo, T. Zeng, M. Zhou and H. Hou, *J. Environ. Chem. Eng.*, 2025, **13**, 115539.
25 M. Imran, A. Z. Abdullah, M. Arishi, S. K. Ali, M. E. Khan, M. Fellah and A. A. Chaudhary, *Ceram. Int.*, 2025, **51**, 44598–44611.
26 W. J. Aziz, M. A. Abid and E. H. Hussein, *Mater. Technol.*, 2020, **35**, 447–451.
27 A. E. D. Mahmoud, K. M. Al-Qahtani, S. O. Alflaij, S. F. Al-Qahtani and F. A. Alsamhan, *Sci. Rep.*, 2021, **11**, 1–13.
28 Y. Yang, D. Xu, Q. Wu and P. Diao, *Sci. Rep.*, 2016, **6**, 1–13.
29 A. M. Eid, A. Fouda, S. E. D. Hassan, M. F. Hamza, N. K. Alharbi, A. Elkelish, A. Alharthi and W. M. Salem, *Catalysts*, 2023, **13**, 348.
30 Md. K. H. Shishir, M. Islam, N. R. Sayeem, N. S. Anam, Md. R. I. Shipon, Md. Rifat, S. Ahmed, Md. Tauhiduzzaman and Md. Ashraful Alam, *Chem. Inorg. Mater.*, 2025, **7**, 100123.
31 P. G. Bhavyasree and T. S. Xavier, *Curr. Res. Green Sustainable Chem.*, 2021, **4**, 100161.
32 A. Fakhri, *Process Saf. Environ. Prot.*, 2015, **93**, 1–8.
33 P. P. Sarma, P. Borah, M. R. Das and P. K. Baruah, *J. Water Proc. Eng.*, 2025, **70**, 107004.
34 P. Adhya, S. Saha Chowdhury, S. De, T. Mondal and M. Kaushal, *Sep. Purif. Technol.*, 2025, **358**, 130279.
35 K. S. W. Sing, D. H. Everett, R. A. W. Haul, L. Moscou, R. A. Pierotti, J. Rouquerol and T. Siemieniewska, *Pure Appl. Chem.*, 1985, **57**, 603–619.
36 A. E. D. Mahmoud, K. M. Al-Qahtani, S. O. Alflaij, S. F. Al-Qahtani and F. A. Alsamhan, *Sci. Rep.*, 2021, (11), 12547.
37 A. A. Farghali, M. Bahgat, A. Enaiet Allah and M. H. Khedr, *Beni-Suef Univ. J. Basic Appl. Sci.*, 2013, **2**, 61–71.
38 G. Sreekala, B. A. Fathima and B. Beena, *Orient. J. Chem.*, 2019, **35**, 1731–1736.

39 A. Giotto dos Santos, T. R. Martins, S. Krishnamurthy, D. Assumpção Bertuol and E. H. Tanabe, *Metals*, 2025, **15**, 56.
40 X. Jiao, Y. Gutha and W. Zhang, *Colloids Surf. B Biointerfaces*, 2017, **149**, 184–195.
41 J. Gao, Q. Lin, T. Yang, Y. chao Bao and J. Liu, *Chemosphere*, 2023, **341**, 139741.
42 H. I. Syeda, S. Muthukumaran and K. Baskaran, *J. Water Proc. Eng.*, 2024, **58**, 104780.
43 S. Rahimi, R. M. Moattari, L. Rajabi, A. A. Derakhshan and M. Keyhani, *J. Ind. Eng. Chem.*, 2015, **23**, 33–43.